International Conference on Computational Methods in Marine Engineering
MARINE 2011
L.Eça, E. Oñate, J. García, T. Kvamsdal and P. Bergan (Eds)

THE EFFECT OF NON-LINEAR FREE SURFACE ON BLUFF BODY VORTEX DYNAMICS AND CONTROL

Serpil Kocabiyik*, Canan Bozkaya† and Gina Reid*

*Department of Mathematics and Statistics
Memorial University of Newfoundland
St. Johns's, NL, Canada A1C5S7
e-mail: serpil@mun.ca, ginar@mun.ca

† Department of Mathematics
Middle East Technical University, Ankara 06531, Turkey
email: canan@mun.ca

Key words: Two-phase viscous incompressible flow, Bluff body, Vortex dynamics and Control, Volume-of-fluid method, Finite volume method

Abstract. A viscous incompressible two-fluid model with a circular cylinder under streamwise oscillations is investigated at a Reynolds number of 200 and at a displacement amplitude of $A = 0.13$ and for the forcing cylinder oscillation frequency-to-natural vortex shedding frequency ratios, $f/f_0 = 1.25$, 1.75, 2.25, 2.75. Finite volume discretization of the special integral form of two-dimensional continuity and unsteady Navier-Stokes equations (when a solid body is present) are performed on a fixed Cartesian grid. Improved volume-of-fluid method is used to discretize the free surface. The study focuses on the laminar asymmetric flow structure transitions in the near wake region and lock-on phenomena at a Froude number of $Fr = 0.4$ and for the cylinder submergence depths, $h = 0.25$, 0.5 and 0.75. The results detail the link between the force and the wake dynamics of the cylinder, and provide some insight into the understanding of active flow control mechanisms on coastal and offshore engineering systems. The code validations in special cases show good comparisons with previous numerical results.

1 INTRODUCTION

The transformation between kinetic and potential energies and the coexistence of viscous and gravity forces at an unknown wavy boundary make the free surface phenomena difficult to study. A great amount of work has been carried to explore the behaviour of free surface vorticity. However, fundamental research is needed in order to understand the interaction of a free surface with bluff body wakes which has been principally the subject

of experimental studies (see e.g., [1], [2]). Such flows are found in ocean engineering applications and undersea technology. Computations of nonlinear viscous free surface problems including cylindrical bodies are relatively few (see e.g., [3, 4]). In this paper two-phase flow problem based on a viscous incompressible two-fluid model with a circular cylinder is investigated numerically. A basic schematic that illustrates the problem is shown in Figure 1. The present two-fluid model involve the fluids in the regions Ω_1 and Ω_2 with densities, ρ_1, ρ_2, and dynamic viscosities, μ_1, μ_2, entering into the domain with uniform velocity U at the inlet and leaving through the outlet boundary. The circular cylinder of

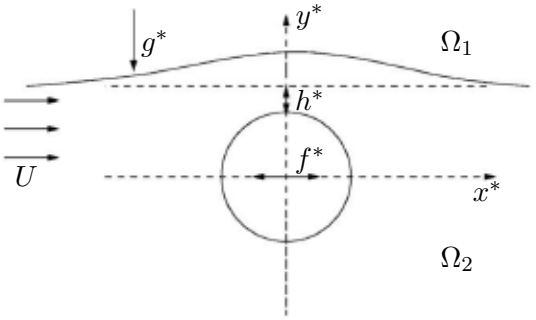

Figure 1: Schematic of the problem.

radius, d, is submerged in the fluid region Ω_2 at the distance h^* below the undisturbed free surface. Initially, an infinitely long circular cylinder whose axis coincides with the z-axis is at rest, and then, at time $t = 0$, the cylinder starts to perform streamwise oscillations about the x-axis. The imposed oscillatory cylinder displacement is assigned by $x(t) = A\cos(2\pi ft)$. The relevant dimensionless parameters are the Reynolds number $R_2 = Ud/\nu_2$ ($R_1 = Ud/\nu_1$); the forcing amplitude of the cylinder oscillations, $A = A^*/d$; the frequency ratio, f/f_0, with $f = df^*/U$ and $f_0 = df_0^*/U$ being the dimensionless forcing frequency of the cylinder oscillation and the natural vortex shedding frequency; the cylinder submergence depth, $h = h^*/d$, and the Froude number, $Fr = U/\sqrt{dg^*}$. Here, $\nu_1 = \mu_1/\rho_1$, $\nu_2 = \mu_2/\rho_2$ are the kinematic viscosities of the fluids in Ω_1 and Ω_1, respectively, f^* is the dimensional forcing frequency of cylinder oscillation, f_0^* is the dimensional natural vortex shedding frequency of a stationary cylinder, g^* is the acceleration due to gravity, $\vec{g}^* = (0,\ g^*,\ 0)$, $t^* = td/U$ is the dimensional time, and t being the dimensionless time. The dimensionless fluid pressure, p, is defined by $p/\varepsilon = p^*/\rho_2 U^2$, where $\varepsilon = \rho_1/\rho_2$ when $\vec{x} \in \Omega_1$, and $\varepsilon = 1$ when $\vec{x} \in \Omega_2$.

2 NUMERICAL MODEL AND ITS VALIDATION

The present paper adopts basically the same two phase flow model and numerical method as that used by Bozkaya *et al.* [4], and only a brief description of points of direct relevance to the computations will be provided here, further details of the implementation can be found in [4]. Versteeg and Malalasekera [5] provide an excellent description of the

finite-volume method on which the computational code is based. The free surface interface is discretized with the volume-of-fluid method due to Hirt and Nichols [6]. Its advection in time is performed based on the strictly mass conserving volume-of-fluid advection method in two dimensional incompressible flows, due to Aulisa *et. al.* [7]. For the moving fluid-body interface the fractional area/volume obstacle representation method due to Hirt and Sicilian [8], and the cut cell method due to Gerrits [9] are employed.

The governing equations are the two-dimensional continuity and the Navier-Stokes equations given by

$$\frac{d\mathbb{V}}{dt} + \int_{\mathbb{A}} (\vec{u} \cdot \vec{n})\, dS = 0, \tag{1}$$

$$\frac{d}{dt}\int_{\mathbb{V}} \vec{u}\, dV + \int_{\mathbb{A}} (\vec{n} \cdot \vec{u})\vec{u}\, dS = -\frac{1}{\varepsilon}\int_{\mathbb{A}\cup\mathbb{I}} p\vec{n}\, dS + \frac{1}{R}\int_{\mathbb{A}\cup\mathbb{I}} \vec{n} \cdot \nabla\vec{u}\, dS + \int_{\mathbb{V}} \vec{F}\, dV \tag{2}$$

where $\mathbb{V}$ and $\mathbb{A}$ are the fractional volume and area, respectively, open to flow within the computational cell, V; $\mathbb{I}$ is the length of the fluid-body interface open to flow; $\vec{u}$ is the dimensionless velocity vector, where $\vec{u} = (u,\ v,\ 0)$; $\vec{n}$ is the outward unit normal vector; S is the control volume boundary. These dimensionless quantities are defined in terms of their dimensional counterparts: $x = x^*/d,\ y = y^*/d,\ u = u^*/U,\ v = v^*/U$;- $V = V^*/d^2,\ S = S^*/d,\ \mathbb{V} = \mathbb{V}^*/d^2,\ \mathbb{A} = \mathbb{A}^*/d,\ \mathbb{I} = \mathbb{I}^*/d$. The external force, $\vec{F} = (-a_1,\ 1/Fr^2 - a_2,\ 0)$, is due to the dimensionless gravity force, $\vec{g} = (0, 1/Fr^2, 0)$, and the dimensionless acceleration of the non-inertial frame of reference, $(-a_1,\ -a_2,\ 0)$. The single set of governing equations (1)-(3) are solved in the flow part of the computational domain, $\Omega = \Omega_1 \cup \Omega_2$, after setting the fluid properties to ρ_1/ρ_2=1/100 and μ_1/μ_2=1/100 (or ν_1/ν_2=1) following the work of Reichl *et. al.* [3]. Therefore, the Reynolds numbers in the fluid regions Ω_1 and Ω_2 are the same ($R \equiv R_1 = R_2$) which is varied by altering the viscosity.

The boundary conditions are no-slip of the fluid on the cylinder surface, $u = 0,\ v = 0$; the uniform stream at the inflow, $u = U - v_1,\ v = -v_2$; and the free slip conditions at the top and bottom boundaries of the computational domain, $\partial u/\partial x = 0,\ v = -v_2$. The well-posed open boundary conditions,

$$\frac{1}{R}\frac{\partial u}{\partial x} + \frac{\bar{h}}{Fr^2} = p, \quad \frac{\partial v}{\partial x} = 0 \tag{3}$$

are enforced at the outflow boundary. Here, v_1 and v_2 are the x- and y-components of the velocity of the non-inertial frame of reference, respectively, and $\bar{h}$ is the height of the fluid at the outflow boundary. The uniform flow is used as the initial condition. It is assumed that at time $t = 0$, the free surface is undisturbed.

Finite volume discretization of the governing equations are performed for two fluid regions Ω_1 and Ω_2 on a fixed Cartesian grid based on the aggregated-fluid approach by describing the behaviour of both fluids using one set of equations (1)-(2). A non-inertial frame of reference is used to eliminate previously reported computational difficulties in

solving the governing equations in an inertial frame of reference which results in pressure spikes (see for example, Kleefsman [10]). A second-order accurate central-difference scheme is used to discretize the governing equations in space in conjunction with first-order explicit forward Euler scheme to advance the numerical solution in time. A cell merging procedure is used to preserve a global second-order accuracy of the spatial discretization. The computational domain size and the number of cells per diameter are the same as that used by Bozkaya *et al.* [4], since these are found to be satisfactory and are checked carefully. The computational domain size and the number of cells per

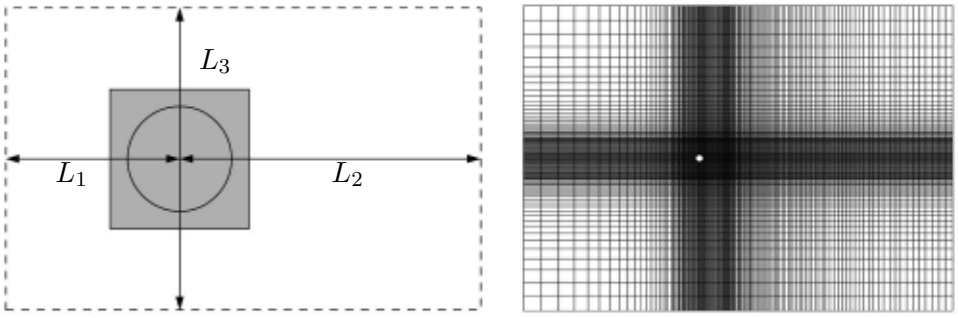

Figure 2: Grid geometry parameters (left). The shaded region is uniform grid region. Grid used for the majority of the simulations (right). It contains 250×190 cells.

diameter are the same as that used by Bozkaya *et al.* [4], since these are found to be satisfactory and are checked carefully. The computational domain geometry is defined with respect to the *mean* position of the cylinder. In the vicinity of the mean cylinder position, the grid has fine resolution and is uniform. Outside of the uniform grid region, the grid expands exponentially towards the four boundaries of the computational domain. The computational grid geometry is defined by specifying the locations of inflow and outflow boundaries, L_1 and L_2, along the x-axis and the location of the top and bottom boundaries, L_3, along the y-axis as shown in Figure 2. For a Reynolds number of 200, this mesh give a natural shedding frequency of $f_0 = 0.198$. This is within 0.1% of the accepted value of $0.197 - 0.199$ as shown in Table 1. In this table, the predicted values of the maximum lift coefficient, $C_{L,max}$; the mean drag coefficient, $\widehat{C_D}$, and the predicted natural shedding frequency, f_0, are displayed using the numerical grid with $L_1 = 20$, $L_2 = 30$, $L_3 = 40$; 60 cells per cylinder diameter and $\Delta t = 0.005$, 0.0075 and 0.01. The predicted present results are in good agreement with previous numerical and experimental studies. Thus, this numerical grid with 60 cells per diameter seems to be sufficient to capture the physical development of the flow in the boundary layer region accurately. The present computations for $R = 200$ are terminated at $t_{\max} = 100$ and 150, in the presence and absence of a free surface (symbolically $h = \infty$), respectively. The choice of these various parameters and the time step, $\Delta t = 0.005$, are the same as that given by Bozkaya *et al.* [4]. The development of the drag coefficient at small values of time is

R	Ref.	f_0	$\widehat{C_D}$	$C_{L,max}$
200	Present ($\Delta t = 0.005$)	0.197239	1.3324	0.682
	Present ($\Delta t = 0.0075$)	0.197239	1.3312	0.681
	Present ($\Delta t = 0.01$)	0.19646	1.3302	0.680
	Poncet [11]	0.199	1.3389	0.70
	Henderson [12]	0.1972	1.3412	-
	De Palma *et al.* [13]	0.19	1.34	0.68

Table 1: The comparison of the predicted natural vortex shedding frequency, f_0; the maximum lift coefficient, $C_{L,max}$; the mean drag coefficients, $\widehat{C_D}$, with the previous numerical results.

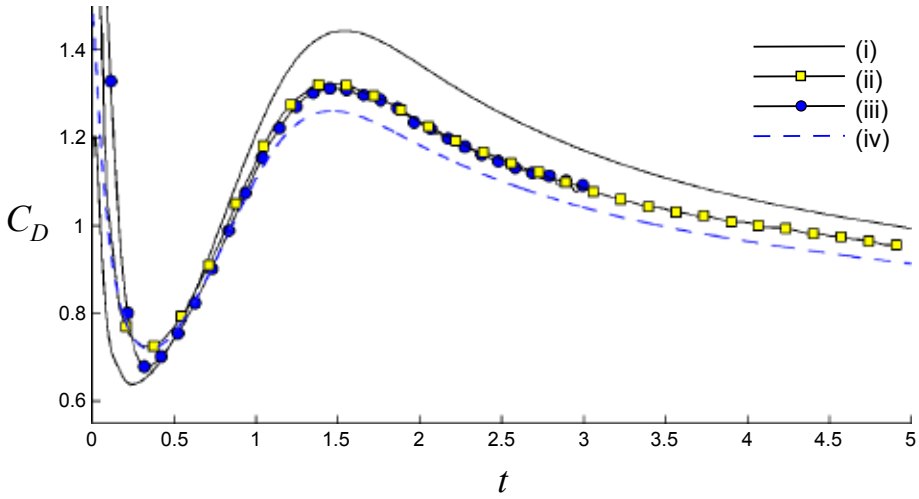

Figure 3: The drag coefficient, C_D, for uniform flow past a stationary cylinder in the absence of a free surface at $R = 550$: (i) Gubanov [16], (ii) Ploumhans and Winckelmans [14], (iii) Li *et al.* [15], (iv) present work.

compared with previous numerical results for uniform flow past a stationary cylinder at $R = 550$ as shown in Figure 3. The predicted drag coefficient values are slightly lower than the ones obtained by Ploumhans and Winckelmans [14] and Li *et al.* [15]. This is due to numerical viscosity introduced by the relatively low-order scheme employed in the present study. This artificial diffusion results in a flow behaving as if it were at a slightly lower Reynolds number, which is consistent with smaller $\widehat{C_D}$ values observed in Table 1. The drag coefficients of Gubanov's [16] single-phase fluid model and the present two-fluid model differ appreciably (about 20%). The present two-phase flow model enables implicit application of boundary conditions at the free surface and uses free slip wall boundary conditions unlike Gubanov's single-phase fluid model and thus produces more accurate results.

3 RESULTS

The present study focuses on the problem of unsteady flow of a viscous incompressible fluid past a oscillating circular cylinder in the presence of a free surface at a Froude number of $Fr = 0.4$. The numerical simulations are carried out in both absence (symbolically $h = \infty$) and presence of a free surface at cylinder submergence depths, $h = 0.25$, 0.5, 0.75, for the case of $R = 200$: $A = 0.13$ and $f/f_0 = 1.25$, 1.75, 2.25, 2.75. The unsteady flow calculations are conducted for the time up to $t = 150$ when $h = \infty$ and up to $t = 100$ when $h = 0.25$, 0.5, 0.75 with the time step size $\Delta t = 0.005$. In all equivorticity patterns that follow, black colours correspond to counterclockwise rotation (positive) and gray colours indicate clockwise rotation (negative). All snapshots that follow, $t = 0T$ corresponds to the instant when the cylinder reaches its maximum displacement, $x(t) = A$. In the pressure contour plots, black and gray colours represent high (positive) and low (negative) pressure regions, respectively. Results indicate that it is possible to generate distinctly different vortex formation modes than that of the well know classical modes observed by Williamson and Roshko [17]. These new modes are the combination of the two, four and five **C(2S)** mode i.e., **C(4S)**, **C(8S)**, **C(10S)** modes.

Table 2 summarizes the effect of free surface inclusion on the flow regimes, the vortex shedding modes and their periods, T_v, for the case $Fr = 0.4$ at $h = 0.25$, 0.5, 0.75 when $f/f_0 = 1.25$, 1.75, 2.25, 2.75. It is evident that the presence of the free surface at $h = 0.25$ seems to break up the periodicity of vortex shedding when $f/f_0 = 1.75$, 2.25. Destabilization of the flow also occurs at $h = 0.5$ when $f/f_0 = 2.75$ and at $h = 0.75$ when $f/f_0 = 1.25$, 2.75, compared to the reference case $h = \infty$. Moreover, the flow shows two different regimes in the presence of free surface for several $h - f/f_0$ combination at $Fr = 0.4$, whereas it becomes periodic/quasi-periodic after the initial transition period for all f/f_0 in the absence of free surface. Moreover, new vortex shedding modes are observed for the quarter-integer values of frequency ratio. These modes are the quasi-locked-on **C(4S)** mode, per $4T$, when $h = 0.25$, $f/f_0 = 1.25$; the quasi-locked-on **C(8S)** mode, per $5T$ (or $9T$), when $h = 0.5$, $f/f_0 = 1.25$ (or $h = \infty$, $f/f_0 = 2.25$); the quasi-locked-on **C(10S)** mode, per $7T$, when $h = \infty$, $f/f_0 = 1.25$. The detailed analysis of the near wake structures will be presented only for the case when $h = 0.25$, $f/f_0 = 1.25$ (full details will be published elsewhere).

The equivorticity patterns and the pressure contours over four periods of cylinder oscillation, $4T$, when $f/f_0 = 1.25$ are displayed in Figure 4 (quasi-periodic state). The vortex shedding mode is the quasi-locked-on **C(4S)** mode, per $4T$, within $7T \leq t \leq 14T$. This mode is the combination of the two classical **C(2S)** modes. The flow becomes non-periodic within $14T < t < 25T$. It is seen from the figure that positive and negative vortices developed in the previous vortex shedding cycle are alternately shed into the downstream of the cylinder at $t \approx T/2$ and $t \approx 3T/2$, respectively. The positive vortex becomes oval shaped with the major axis laying parallel to the free surface. Then, a single positive vortex formed by the coalescence of a pair of positive vortices over $T/2 \leq t \leq 3T/2$

	$h = 0.25$		$h = 0.5$		$h = 0.75$		$h = \infty$	
f/f_0	Mode	T_v	Mode	T_v	Mode	T_v	Mode	T_v
1.25	**C(4S)*** $7T \le t \le 14T$; non-locked $15T < t < 24T$	$4T$	**C(8S)*** $3T \le t \le 13T$; non-locked $14T < t < 24T$	$5T$	non-locked	-	**C(10S)***	$7T$
1.75	non-locked	-	**C(2S)*** $13T \le t \le 19T$; non-locked $20T < t < 34T$	$2T$	**C(P+S)*** $6T \le t \le 12T$ non-locked $13T < t < 34T$	$2T$	**2P**	$2T$
2.25	non-locked	-	**C(2S)*** $4T \le t \le 22T$; non-locked $23T < t < 44T$	$2T$	**C(2S)*** $4T \le t \le 19T$; non-locked $20T < t < 44T$	$2T$	**C(8S)***	$9T$
2.75	**C(2S)*** $19T \le t \le 27T$; non-locked $28T < t < 54T$	$4T$	non-locked	-	non-locked	-	**C(P+S)***	$3T$

Table 2: The effect of the free surface inclusion at $Fr = 0.4$ and $h = 0.25$, 0.5, 0.75, ∞, on vortex shedding modes and their periods, T_v, at $Re = 200$: $A = 0.13$, $f/f_0 = 1.25$, 1.75, 2.25, 2.75. The superscript "*" denotes quasi-locked-on modes.

becomes detached from the lower part of the cylinder at $t \approx 5T/2$. Finally, a negative vortex is shed into the upper vortex shedding layer at $t \approx 3T$, by the development and the propagation of a positive vortex from the free surface. However, this vortex remains attached to the free surface. Thus, the cylinder alternately sheds two single vortices from each sides over one vortex shedding cycle, $T_v = 4T$, which results in the quasi-locked-on **C(4S)** mode. The pressure plots shows that when the cylinder reaches its maximum displacement at $t = 0T$, the high pressure region is associated with the stagnation region while the low pressure concentrates rear and through the downstream of the cylinder where both positive and negative vortices are located. It is also noted that the shedding of the positive vortices at $t \approx T/2$ and $t \approx 5T/2$ seems to induced a local free surface rising and thus leads to the appearance of sufficiently high pressure region near the curved free surface interface. On the other hand, the lowest pressure region concentrated rear and below of the cylinder at $t = 0T$ switches to the above of the cylinder when the free surface falls down sufficiently in this region.

Figure 5 displays the effect of cylinder submergence depth, h, and the frequency ratio, f/f_0, on the equivorticity patterns. The reference case $h = \infty$ is also presented to

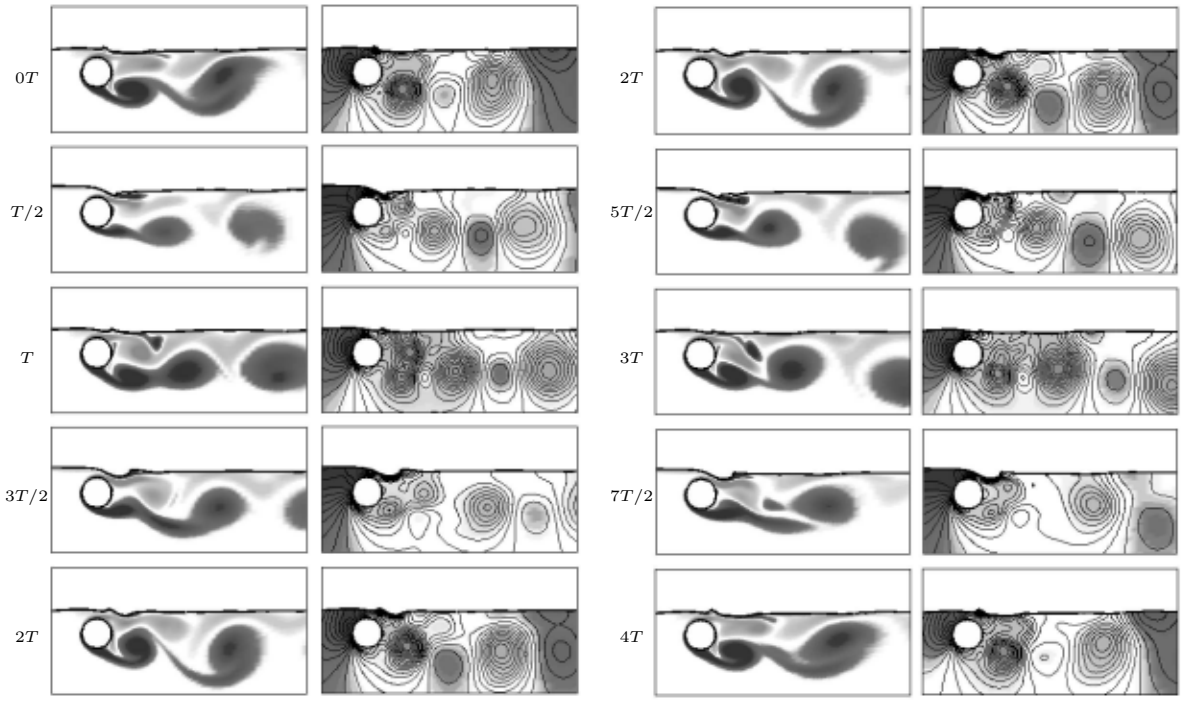

Figure 4: The equivorticity patterns (left) and pressure contours (right) in the near wake over four periods of cylinder oscillation, $4T$, at $R = 200$: $A = 0.13$, $f/f_0 = 1.25$ when $Fr = 0.4$ and $h = 0.25$ [$T \approx 4.04, 32.32 \leq t \leq 48.48 :\ (8T, 12T)$]. The quasi-locked-on $\mathbf{C}(\mathbf{4S})$ mode, per $4T$, is observed.

demonstrate the changes the vorticity undergoes in the near wake of the cylinder with the inclusion of free surface. It is noted that for the periodic/quasi-periodic cases the snapshots are taken over the time interval in which the flow reaches to a periodic/quasi-periodic state whereas in non-periodic cases the commonly appearing equivorticity plots at $x(t) = A$ (within the time interval $0 < t \leqslant 100$) are drawn. It is obvious that free surface undergoes considerable deformations resulting in localized interface sharpening and wave breaking as h decreases from 0.75 to 0.25 and f/f_0 increases from 1.25 to 2.75. This yields the formation of a considerable amount of opposite signed vorticity from the free surface for all f/f_0. This vorticity interferes with the development of negative vorticity in the upper vortex shedding layer especially at small cylinder submergence depths, $h = 0.25$, 0.5. The near wake structures of the vorticity at $h = 0.5$, 0.75 for each f/f_0 is similar to the reference case $h = \infty$, whereas a significant change is observed at the smallest submergence depth, $h = 0.25$. At each cylinder submergence depth, h, the shed negative vortices seem to be lifted up toward the free surface aided by the propogation of positive vorticity into the upper vortex shedding layer. As a result, these negative vortices dissipate rapidly, and become weak, as they approach the free surface. Hence, the vortex shedding becomes more skew symmetric in favour of the positive vortices as h decreases from ∞ to 0.25. It can be seen that the major axes of the negative vortices

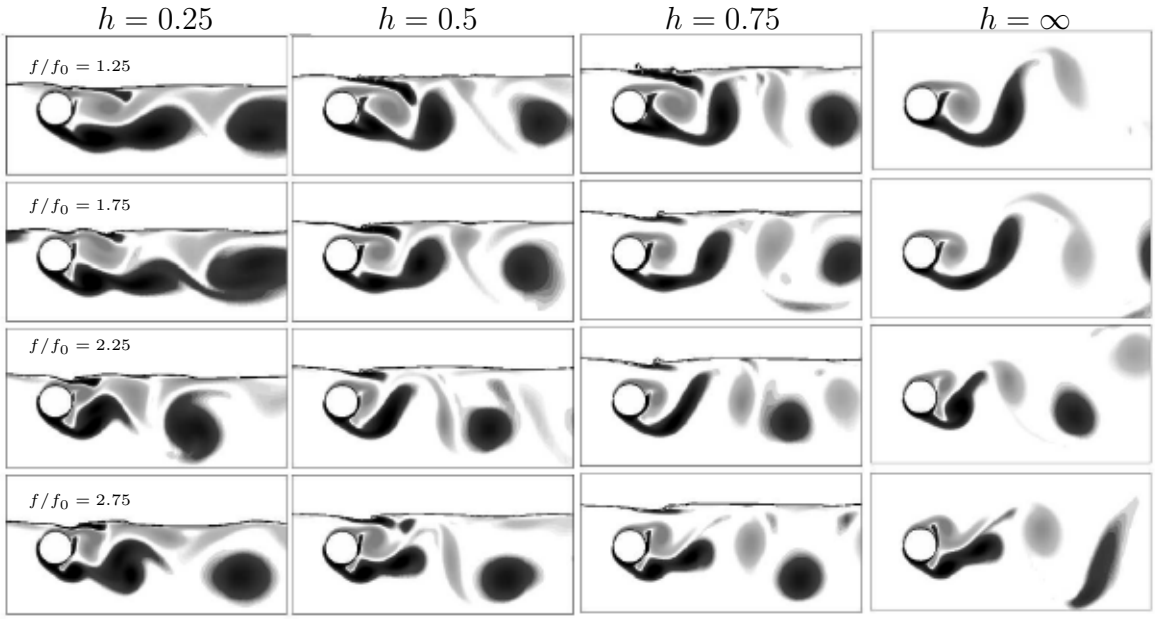

Figure 5: The effect of the cylinder submergence depth, h, and the frequency ratio, f/f_0, on the equivorticity patterns at $R = 200$: $A = 0.13$, $Fr = 0.2$.

downstream of the cylinder tend to lie perpendicular to the free surface for the larger cylinder submergence depths, $h = 0.5, 0.75, \infty$. On the other hand, the major axes of the negative vortices at $h = 0.25$ tend to lie more parallel to the free surface. This is a result of the strong interaction with the free surface and the rapid diffusion of these vortices after contact is made. Both cases also apply to the shed positive vortices in the downstream of the cylinder, except that the positive vortices do not primarily interact with the free surface. In general, the vortex formation length remains consistent as h decreases from ∞ to 0.25 for all f/f_0, except the cases $h = 0.25$ when $f/f_0 = 1.25$, 1.75, 2.75 (maximum increase $\approx 23\%$). On the other hand, an increase in f/f_0 from 1.25 to 2.25 results in a decrease in vortex formation length (maximum by $\approx 44\%$) for all cylinder submergence depths.

Figure 6 illustrates the link between the lift coefficient and the corresponding vorticity patterns and pressure contours. In this figure the lift coefficient, C_L, is shown along with the cylinder displacement, $x(t)$, and the images of vorticity and pressure are obtained at the time indicated by dots. The lift trace contained three dominant peaks at $h = 0.25$ shows a periodic behaviour over two periods of cylinder oscillation, $2T$, resulting in a quasi-locked-on $\mathbf{C}(\mathbf{4S})$ vortex shedding mode. The lift trace progresses from the one contained three peaks per $2T$ to a near sinusoidal trace with an increase in h from 0.25 to 0.5 and finally to 0.75. The disapperance of the secondary peaks following the increase in the cylinder submergence depth leads to the development of the quasi-locked-on $\mathbf{C}(\mathbf{8S})$

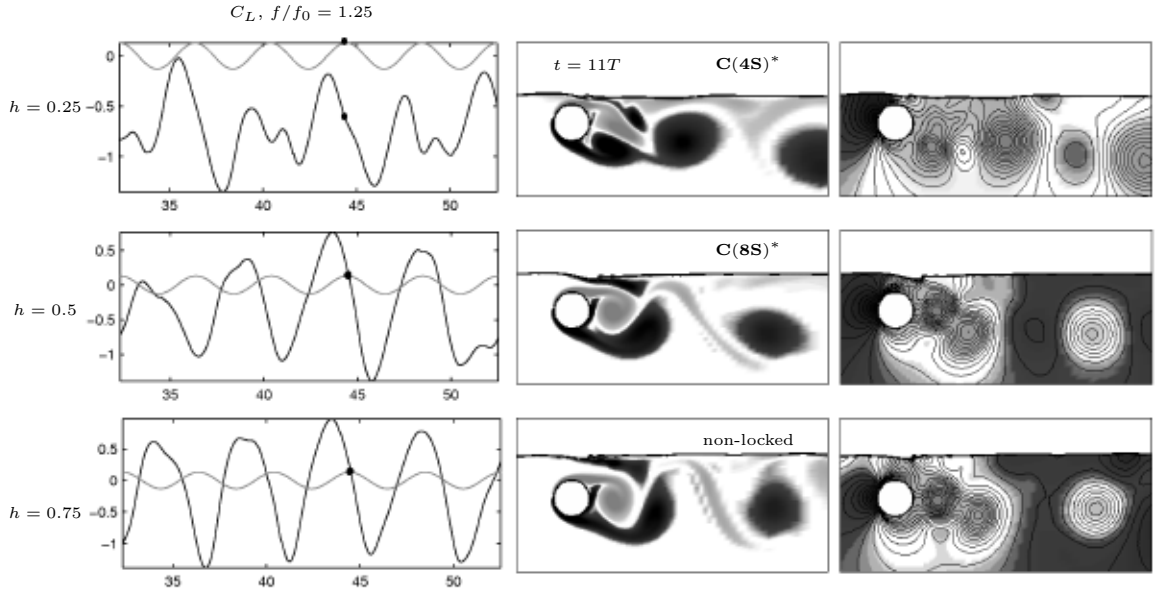

Figure 6: The lift coefficient (black), C_L, along with cylinder displacement (gray), $x(t)$ (left); and the corresponding equivorticity patterns (middle) and pressure distributions (right) at $R = 200$: $A = 0.13$, $f/f_0 = 1.25$, $Fr = 0.4$ when $h = 0.25$, 0.5, 0.75 from above to bottom. Dots indicate point at which images of vorticity and pressure are obtained, ($T \approx 4.04$, $t = 11T$). The superscript "*" denotes quasi-locked-on modes.

mode at $h = 0.5$. Further increase in h to 0.75 causes a transition into the non-periodic state although the vorticity and pressure images show almost similar patterns at both $h = 0.5$ and $h = 0.75$ unlike the case when $h = 0.25$. The high pressure region is concentrated upper left side of the cylinder at $h = 0.25$, and is shifted towards the front stagnation point as h increases. On the other hand, the low pressure region concentrated in the lower vortex shedding layer at $h = 0.25$ moves in the counterclockwise direction and is mostly confined at the back of the cylinder at $h = 0.5$, 0.75, giving a positive C_L.

4 CONCLUSION

The problem of two-dimensional uniform viscous flow past a circular cylinder subject to forced streamwise oscillations beneath a free surface is investigated numerically based on a two fluid model. The numerical simulations are carried out at Reynolds number of $R = 200$ and Froude number of $Fr = 0.4$: $A = 0.13$ and $h = 0.25$, 0.5, 0.75 when $f/f_0 = 1.25, 1.75, 2.25, 2.75$. The results shows two different flow regimes. Flow either becomes non-periodic in the whole time interval or becomes periodic (or quasi-periodic) over several periods of cylinder oscillation, and then a transition into the non-periodic state occurs. A similar phenomena has been reported in the experimental study by Cetiner and Rockwell [2] for the case of cylinder subject to streamwise oscillations in uniform flow in the presence of the free surface. On the other hand, in the absence of free

surface the flow shows periodic/quasi-periodic behaviour over the whole time interval after the initial transition period for each f/f_0. The resulting new modes are the combination of the two, four and five **C**(**2S**) classical modes i.e., **C**(**4S**), **C**(**8S**) and **C**(**10S**) modes. It is also observed the near wake structures differs depending on the fluctuation of the lift coefficient, C_L, as the cylinder submergence depth, h, increases (see Figure 6). As h decreases from 0.75 to 0.25, the almost sinusoidal fluctuation of C_L for $f/f_0 = 1.25$ changes to one that contains alternative secondary peaks. Moreover, a phase shift between C_L and $x(t)$ and a change in the value of C_L from negative to positive occur with an increase in h from 0.25 to 0.75. All of these changes in C_L result in a transition in the vortex shedding mode (from **C**(**4S**) to non-loked-on state for $f/f_0 = 1.25$) and a displacement of the high and low pressure fields around the cylinder.

5 ACKNOWLEDGEMENT

The financial support for this research is provided by the Natural Sciences and Engineering Research Council of Canada.

REFERENCES

[1] Sheridan, J., Lin, J.-C. and Rockwell, D. Flow past a cylinder close to a free surface, *J. Fluid Mech.* (2007) **330**: 1-30.

[2] Cetiner, O. and Rockwell, D. Streamwise oscillations of a cylinder in a steady current. Part 2: Free-surface effects on vortex formation and loading. *J. Fluid Mech.* (2001) **427**:29-59.

[3] Reichl, P., Hourigan, K. and Thompson, M.C. Flow past a cylinder close to a free surface. *J. Fluid Mech.* (2005) **533**: 269-296.

[4] Bozkaya, C., Kocabiyik, S., Mironova, L.A. and Gubanov, O.I. Streamwise oscillations of a cylinder beneath a free surface: Free surfacer effects on vortex formation modes. *J. Comput. Appl. Math.* (in press).

[5] Versteeg, H. K. and Malalasekera, W. *An Introduction to Computational Fluid Dynamics. The Finite Volume Method*, Longman Scientific and Technical, (1995).

[6] Hirt, C.W. and Nichols, B.D. Volume of fluid method for the dynamics of free boundaries. *J. Comput. Phys.* (1981) **39**: 201-225.

[7] Aulisa, E., Scardovelli, R., Manservisi, S. and Zaleski, S. A geometrical area-preserving volume of fluid advection method. *J. Comput. Phys.* (2003) **192**: 355-364.

[8] Hirt, C.W. and Sicilian, J.M. *A porosity technique for the definition of obstacles in rectangular cell meshes*, Proceedings of the 4^{th} International Conference on Ship Hydrodynamics, Washington, District of Columbia, (1985).

[9] Gerrits, J. *Dynamics of liquid-filled spacecraft*, PhD Thesis, University of Groningen, (2001).

[10] Kleefsman, K.M.T. *Water impact loading on offshore structures. A numerical study.* PhD thesis, University of Groningen, (2005).

[11] Poncet, P. Topological aspects of three-dimensional wakes behind rotary oscillating cylinders. *J. Fluid Mech.* (2004) **517**:27-53.

[12] Henderson, R.D. Nonlinear dynamics and pattern formation in turbulent wake transition. (1997) *J. Fluid Mech.* **352**:65-112.

[13] De Palma, P. Tullio, M.D., Pascazio, G. and Napolitano, M. An immersed-boundary method for compressible viscous flows. *Comput. Fluids* (2006) **35**:693-702.

[14] Ploumhans, P. and Winckelmans, G.S. Vortex methods for high-resolution simulations of viscous flow past bluff bodies of general geometry. *J. Comput. Phys.* (2000) **165**:354-406.

[15] Li, Y., Shock, R., Zhang, R. and Chen, H. Numerical study of flow past an impulsively started cylinder by the lattice-Boltzmann method. *J. Fluid Mech.* (2004) **519**:273-300.

[16] Gubanov, O.I. *Design of CFD code using high level programming paradigms: Free surface flows with arbitrarily moving rigid bodies*, MSc thesis, Memorial University of Newfoundland, (2006).

[17] Williamson, C.H.K. and Roshko, A. Vortex formation in the wake of an oscillating cylinder. *J. Fluid and Struct.*, 2:355–381, 1988.